

## DIGITAL REPRESENTATION OF A LOAD CELL

C. L. Giusca<sup>1</sup>, S. Goel<sup>2</sup>, I. Llavori<sup>3</sup>, R. Kumme<sup>4</sup>, O. Baer<sup>5</sup>, A. Prato<sup>6</sup>, A. Germak<sup>7</sup>

Cranfield University, Cranfield, Bedfordshire, United Kingdom, <sup>1</sup>c.giusca@cranfield.ac.uk  
London South Bank University, London, United Kingdom, <sup>2</sup>goels@lsbu.ac.uk  
Mondragon Unibertsitatea, Mondragón, Spain, <sup>3</sup>illavori@mondragon.edu  
Physikalisch-Technische Bundesanstalt, Braunschweig, Germany  
<sup>4</sup>rolf.kumme@ptb.de, <sup>5</sup>oksana.baer@ptb.de  
INRiM – National Institute of Metrological Research, Turin, Italy  
<sup>6</sup>a.prato@inrim.it, <sup>7</sup>a.germak@inrim.it

### Abstract:

Industry 4.0 (I4.0) revolution provides new avalanche of opportunities in the arena of manufacturing and metrology. To take advantage of this opportunity, EMRP 18SIB08 ComTraForce project began the development of *digital constructs* necessary for a Digital Twin of a load cell that allows, in real time, to predict, optimise and maintain desired functionality throughout the device lifetime. Specifically, its project team has been working on developing digital constructs based on experimentally validated finite element models in conjunction with analytical models. The work provides new avenues in establishing force measurement standards.

**Keywords:** force; traceability; digital twin; load cell; finite element modelling

### 1. INTRODUCTION

Load cell measurements are affected by a variety of error sources, and it is envisaged that the development of a digital twin (DT) [1] of the load cell in the I4.0 context [2] can help with reliability and accuracy of the measurements. To achieve this, comprehensive digital constructs of the load cell, which go beyond measurement uncertainty estimations based on simple measurement models, are required. The development of finite element models (FEM) is pivotal to understand the load cell behaviour under cyclic measurement conditions and, subsequently, to establish the effect of creep or fatigue on the output of load cells.

Here we present the initial stages of FEM construction of a 20 kN load cell. The detailed design of the load cell is described elsewhere [3]. This paper focuses mainly on the development of the DT constructs. The results obtained from ABAQUS [4] FEA static implicit solver and an analytical solution were compared with the calibration data of the sensor in accordance with the ISO 376:2011 [5].

### 2. DESCRIPTION OF THE WORK

Figure 1 presents a schematic drawing of the load cell, relative position of the strain gauges (force and bending) and temperature sensor, as well as typical boundary condition used in ABAQUS.

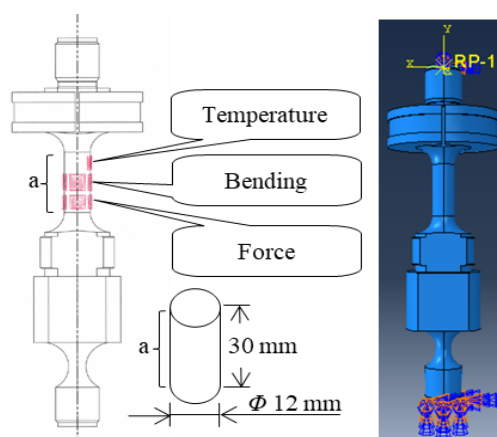


Figure 1: Left - Load cell schematic and the nominal position of the strain gauges. Right - ABAQUS boundary conditions example

Four strain gauges measuring the longitudinal (L) and transversal (T) strains were connected in a Wheatstone bridge configuration as shown in Figure 2. The four strain gauges were mounted at 90° to each other on the body of the dynamometer.

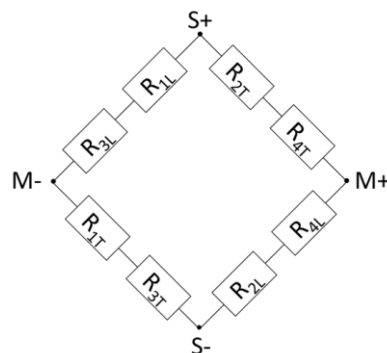


Figure 2: Wheatstone bridge configuration of the strain gauges used for the force measuring setup: S - source, M - measurement

The longitudinal and transversal strain measurements correspond to axial  $\varepsilon_v$  and radial strain  $\varepsilon_r$ , respectively. As such, the millivolt per volt output of the bridge ( $I$ ) can be expressed using equation (1):

$$I = 1000 \times \left( \frac{R_{1L} + R_{3L}}{R_{1L} + R_{3L} + R_{1T} + R_{3T}} - \frac{R_{2T} + R_{4T}}{R_{2L} + R_{4L} + R_{2T} + R_{4T}} \right) \quad (1)$$

On the basis that the resistance ( $R$ ) of the strain gauge is equal to:

$$R = R_0(1 + k\varepsilon) \quad (2)$$

where  $R_0$  is the nominal value of the sensor resistance and  $k$  is the gauge factor.

The equivalent analytical solution to the equation (1) is given by:

$$I = 1000 \times \frac{k\varepsilon(1 + \nu)}{2 + k\varepsilon(1 - \nu)} \quad (3)$$

where  $\nu$  is the Poisson's ratio and  $\varepsilon$  is the analytical axial (longitudinal) strain, which can be calculated as:

$$\varepsilon = \frac{4F}{E\pi d^2} \quad (4)$$

where  $F$  is the applied force,  $E$  is the Young's modulus and  $d$  is the diameter of the dynamometer.

## 2.1. Dynamometer Meshing and Data Processing

Figure 3 shows the meshing conditions of the dynamometer in ABAQUS. The FEM simulations were run with a 2.5 mm distance between nodes (white circles in Figure 3 left). A 10-node modified quadratic tetrahedron (C3D10M) element was used in this study and implicit analysis was chosen. The 2.5 mm distance between the nodes was selected to provide optimal execution time on a desktop computer. An additional simulation was performed by considering the distance between the nodes as 1 mm.

The dynamometer had the properties of a steel alloy: Young's modulus 200 GPa and Poisson's ratio 0.3.

To help with the ease of data collection and postprocessing, the surface of the central part dynamometer on which the strain gauges were mounted was seeded in such way that includes 30 elements (here defined as the space between two seeds) in the axial direction and 36 circumferentially (in Figure 3 the surface edge

seeds are represented by the purple triangles). This configuration of surface seeds allows to collect the spatial displacements ( $U_1, U_2, U_3$ ) at the surface nodes in all three orthogonal directions (X, Y, Z) and their associated positions (in mm), at every 1 mm (nominally) along the axis of the dynamometer and  $10^\circ$  radially (or every 1 mm nominally) along the circumference, hence a set of  $36 \times 31$  (1116) surface nodes.

Figure 3 right presents the ABAQUS meshing result of the dynamometer. Worth mentioning that that the size of the strain gauges is larger than the distance between surface nodes (a ratio approximately of 2:1), however, denser sampling can be used to characterise in more detail the dynamometer response.

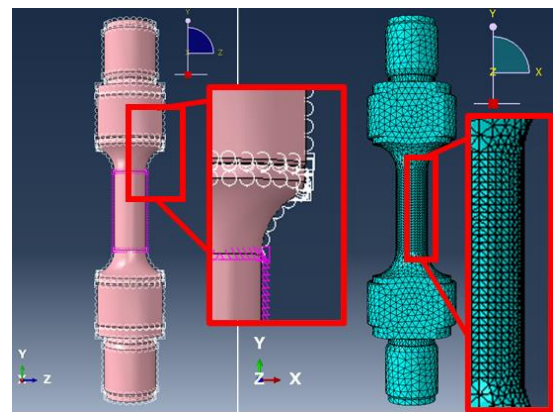


Figure 3: Example of seeding (left) and meshing (right) of the dynamometer

The data was collected along a path that included the surface nodes starting with the top radial data and gradually going down along axial direction of the dynamometer and stored in an Excel file (.xls), which was imported in MATLAB (version R2021b Update3) for further processing and analysis. The FEM spatial displacement results stored in the excel files comprised of  $6 \times (n + 1)$  columns and 1116 rows,  $n$  representing the number of loading increments and "+1" to allow storing the data representing the un-loaded state of the dynamometer (0 N).

A diagrammatic indication of the surface nodes of the dynamometer is presented in Figure 4.

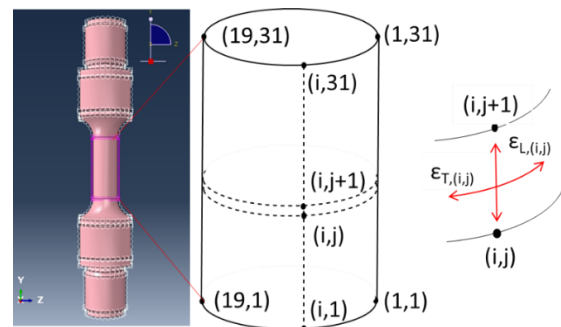


Figure 4: Diagrammatic indication of the surface nodes position on the body of the dynamometer

The longitudinal strain ( $\varepsilon_{L,(i,j)}$ ) - i.e. in the axial direction - of a surface between four adjacent surface nodes was calculated using equation (5).

$$\varepsilon_{L,(i,j)} = \frac{U_{2,(i,j+1)} - U_{2,(i,j)}}{\Delta Y} \quad (5)$$

where  $\Delta Y$  is nominal axial distance between these two axial nodes, and indices  $i$  and  $j$  range from 1 to the number of nodes sampled on the circumference (36) and axial number of nodes less 1 (30), respectively.

At each surface node, the radial strain was calculated as the ratio between the square root of the quadratic sum of the node's displacements along the X and Z direction,  $U_1$  and  $U_3$  respectively, and the diameter of the dynamometer, as shown in equation (6).

$$\varepsilon_{R,(i,j)} = \frac{2 \times \sqrt{U_{1,(i,j)}^2 + U_{3,(i,j)}^2}}{d} \quad (6)$$

where  $i$  and  $j$  range from 1 to the number of nodes sampled on the circumference (36) and axially (31), respectively.

The transversal strain ( $\varepsilon_{T,(i,j)}$ ) was calculated using equation (7).

$$\varepsilon_{T,(i,j)} = \frac{\varepsilon_{R,(i,j+1)} + \varepsilon_{R,(i,j)}}{2} \quad (7)$$

where indices  $i$  and  $j$  range from 1 to 36 and from 1 to 30, respectively.

In the following step, equation (1) was used to derive the equivalent mV/V bridge output using the FEM ( $I_{FEM}$ ) longitudinal and transversal strain results.

$$I_{FEM} = 1000 \times \left[ \frac{2 + k(\varepsilon_{L,(i,j)} + \varepsilon_{L,(i,j+18)})}{4 + k(\varepsilon_{L,(i,j)} + \varepsilon_{L,(i,j+18)} + \varepsilon_{T,(i,j)} + \varepsilon_{T,(i,j+18)})} - \frac{2 + k(\varepsilon_{T,(i,j+9)} + \varepsilon_{T,(i,j+25)})}{4 + k(\varepsilon_{L,(i,j+9)} + \varepsilon_{L,(i,j+25)} + \varepsilon_{T,(i,j+9)} + \varepsilon_{T,(i,j+25)})} \right] \quad (8)$$

## 2.2. Strain Gauge Meshing and Data Processing

The force strain gauges were implemented in ABAQUS as a sandwich of three thin foils (glue, backing and foil) of 6 mm by 6 mm, positioned on the body of the dynamometer using a type "tie" constraint, with the following properties: Young's modulus of 3.45 GPa, 2.96 GPa and 159 GPa, respectively; Poisson's ratio of 0.3 for glue and backing, and 0.3 for the foil.

The FEM simulations were run with a 0.5 mm distance between nodes (resulting in 650 nodes on each surface of the foil 26 by 25 grid). A 10-node

quadratic tetrahedron element (C3D10) was used in this study and implicit analysis was chosen.

The spatial displacements ( $U_1, U_2, U_3$ ) at the surface nodes of the foils and their associated positions (in mm), were collected in a similar method to the one presented in the previous section.

However, the equivalent sensors output was calculated using equation (9).

$$I_{FEM-SENS} = 1000 \times \left[ \frac{2 + k(\varepsilon_{L1,(i,j)} + \varepsilon_{L3,(i,j)})}{4 + k(\varepsilon_{L1,(i,j)} + \varepsilon_{L3,(i,j)} + \varepsilon_{T1,(i,j)} + \varepsilon_{T3,(i,j)})} - \frac{2 + k(\varepsilon_{T2,(i,j)} + \varepsilon_{T4,(i,j)})}{4 + k(\varepsilon_{L2,(i,j)} + \varepsilon_{L4,(i,j)} + \varepsilon_{T2,(i,j)} + \varepsilon_{T4,(i,j)})} \right] \quad (9)$$

where the numbers after L and T indices indicate the sensor number.

## 3. RESULTS

### 3.1. Dynamometer with No Sensors

Here, the FEM compression results at 20 kN for 1 mm and 2.5 mm distance between the dynamometer nodes and two loading conditions, concentrated force - Figure 5 a), and pressure - Figure 5 b), is reported.

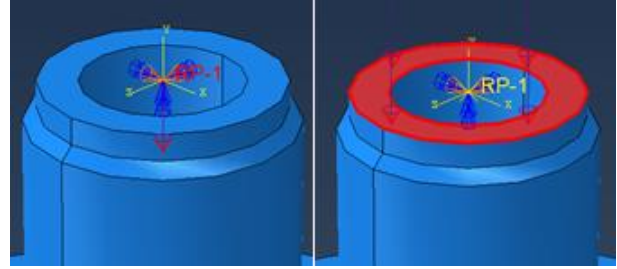


Figure 5: Loading conditions: left) Concentrated force case study; right) Pressure case study

Figure 6a shows a cylindrical plot of all the errors in mV/V between the FEM results at 2.5 mm ( $\times$ ) and 1 mm ( $\circ$ ) meshing distance for concentrated force case study and analytical solution. The magnitude of these errors decreases from approximately 32  $\mu\text{V/V}$  for both meshing distances at the far ends of the sampled area on the dynamometer to below 0.05  $\mu\text{V/V}$  and 0.03  $\mu\text{V/V}$  around the middle of the dynamometer for 2.5 mm and 1 mm meshing distance, respectively.

The standard deviation calculated at each axial position decreases from 1.5  $\mu\text{V/V}$  to 1.7 nV/V. As shown in Figure 6b, the mean errors at each axial position between the FEM results and analytical solution are larger than their associated standard deviations. However, the difference between the average mV/V results for 2.5 mm and 1 mm node distance was larger than their combined standard

deviation only in the middle 12 mm of the dynamometer, see Figure 7.

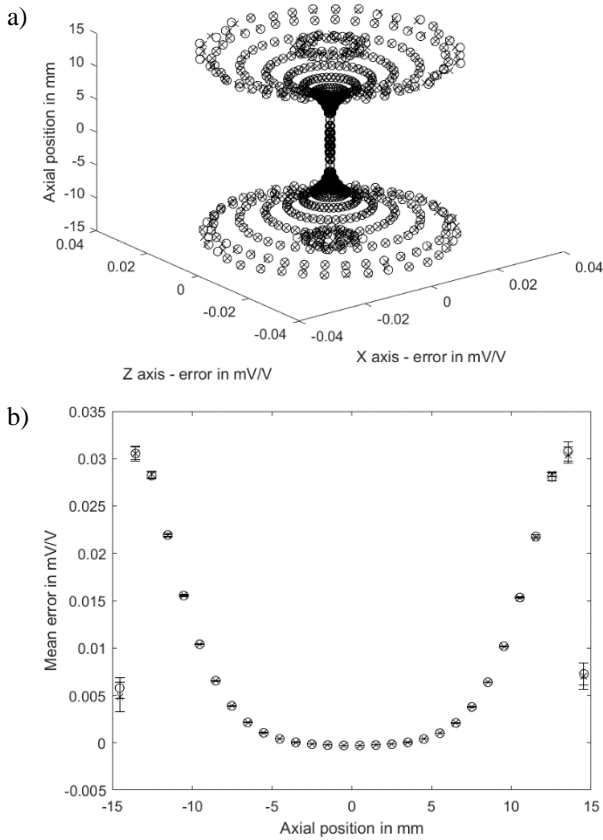


Figure 6: Error maps between FEM compression results at 20 kN, 2.5 mm (x) and 1 mm (o), and the analytical solution in the concentrated force case study: a) all data; b) means and standard deviations (error bars) at each axial position. Axial positions are relative to the middle of the dynamometer

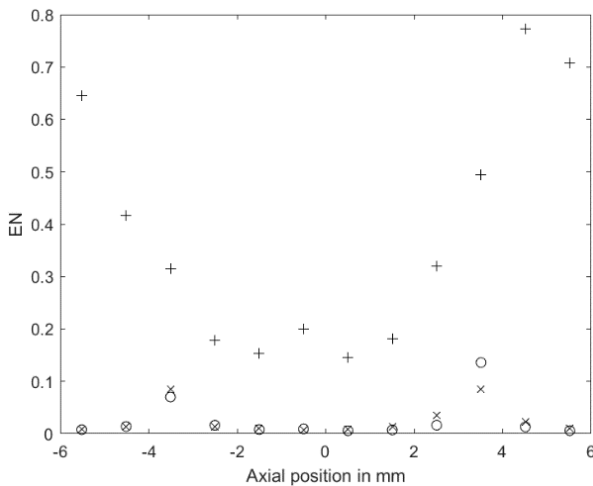


Figure 7: Concentrated force case study at 20 kN – EN is ratio between the standard deviation and the absolute mean error: (x) 2.5 mm nodes distance FEM result relative to the analytical solution, (o) 1 mm and the analytical solution and (+) errors between the two nodes distance FEM results. Axial positions are relative to the middle of the dynamometer

Whilst there are no significant differences between the pressure case study and the

concentrated force, the smallest absolute difference between FEM and analytical solution drops to 0.7 nV/V. The pressure case study provides smaller absolute errors in the central 6 mm of the dynamometer as shown in Figure 8.

Despite such small differences between the two test cases and analytical solution, there is a significant difference between the two of them, as shown in Figure 9. The difference in mV/V is almost constant in the bottom 20 mm.

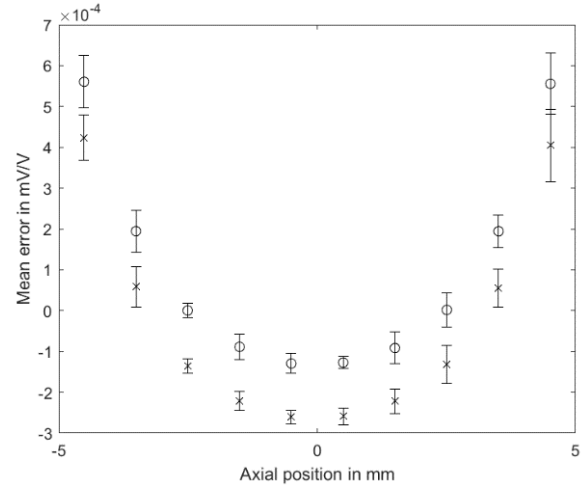


Figure 8: Means and standard deviations ( $\times 10$ ), at the central axial position on the dynamometer, of the errors between the pressure case and the analytical result (o), and the concentrated force and the analytical result (x). All data reported for compression at 20 kN

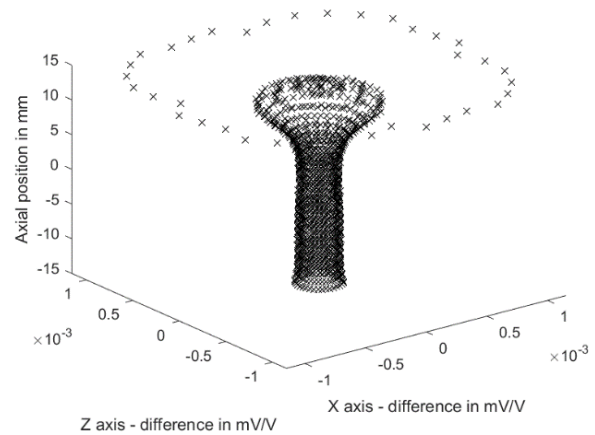


Figure 9: Difference between FEM results for concentrated force and pressure case study at 20 kN and 2.5 mm node distance

As the FEM mV/V response is derived the longitudinal and radial strain, further plots including the relative mean errors between the FEM and analytical results along the axis of the dynamometer and of the relative errors in the middle of the dynamometer are presented in Figure 10a and Figure 10b respectively.

The FEM dynamometer force response is reported for 2.5 mm distance between the nodes and for a range of compression forces ranging from (0 to 20) kN in 10 % increments, and compared

with the real sensor calibration results, which was performed at PTB according to ISO 376:2011. Figure 11a presents the relative mean errors between the FEM results and analytical results, as well as the relative difference between the mean calibration results of the sensor and the analytical solution. Figure 11b presents only the non-linearity errors of the FEM and calibration results.

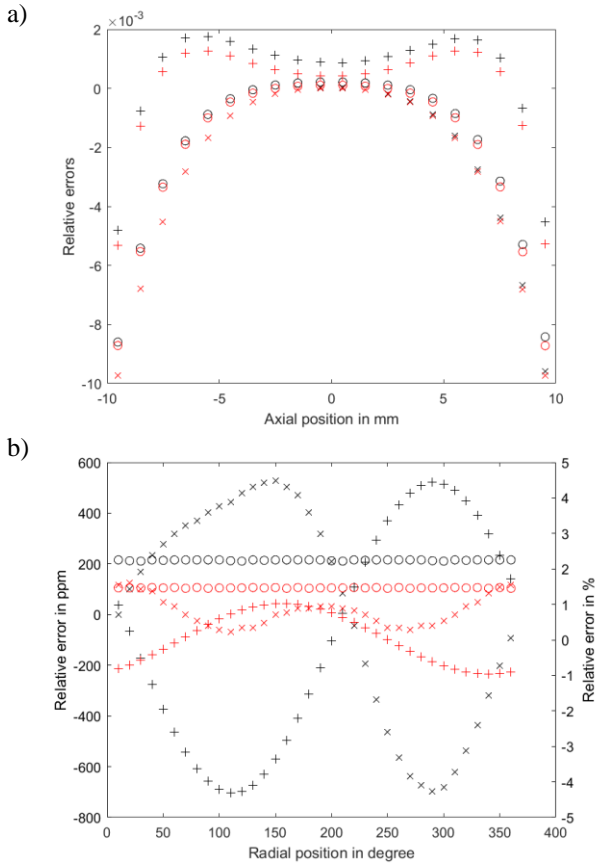


Figure 10: a) Relative mean errors between FEM and analytical results along the axis of the dynamometer; b) Relative errors between FEM and analytical in the middle of the dynamometer (secondary axis in % for radial strain only). Legend: (x) axial strain, (+) radial strain, (o) mV/V indication, black - concentrated force, and red - pressure case study. All data reported for compression at 20 kN and 2.5 mm node distance

Unlike the sensor calibration results, the FEM relative differences from analytical solution do not vary as function of applied force and are just below 0.2 %. Apart from a second order force error (non-linearity), the calibration results are approximately 5.8 % different.

### 3.2. Dynamometer with Sensors

Figure 12 presents the difference between the dynamometer FEM results in mV/V with the strain gauges and without (pressure loading conditions, 20 kN and 2.5 mm node distance).

The errors vary from a couple of parts per million at the top end of the dynamometer (15 mm axial position in Figure 12) to about 0.4 % around

position on the strain gauges. However, the sensor output was found to be noisy and with large errors around the edges of the sensors.

For comparison, the relative errors of the mV/V output of the dynamometer at 6.5 mm below its centre and the average sensors output calculated from all the results obtained between 0.5 mm above and below that position are shown in Figure 13.

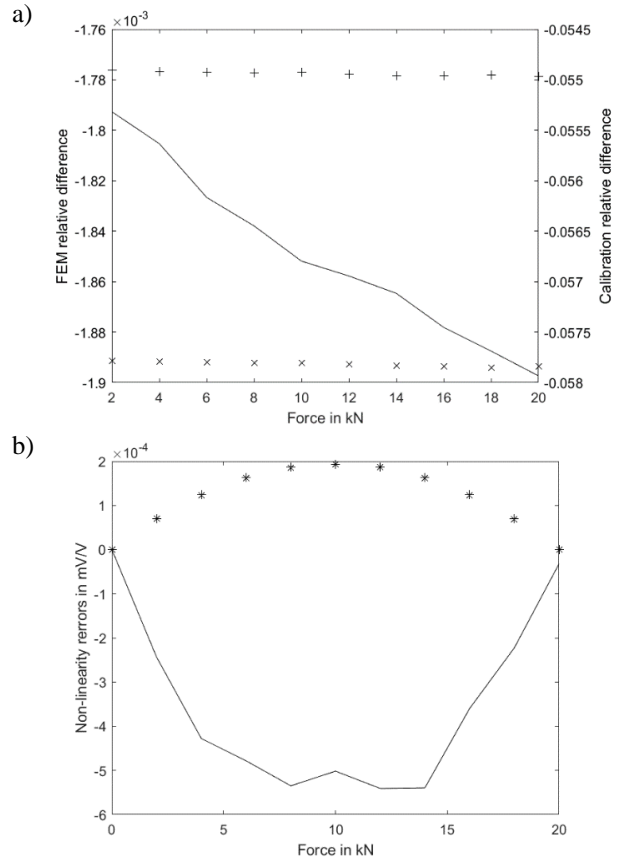


Figure 11: a) Mean relative difference from analytical results 7 mm; b) mean non-linearity errors. Legend: (x) FEM pressure case, (+) FEM concentrated force, continuous line - mean calibration results

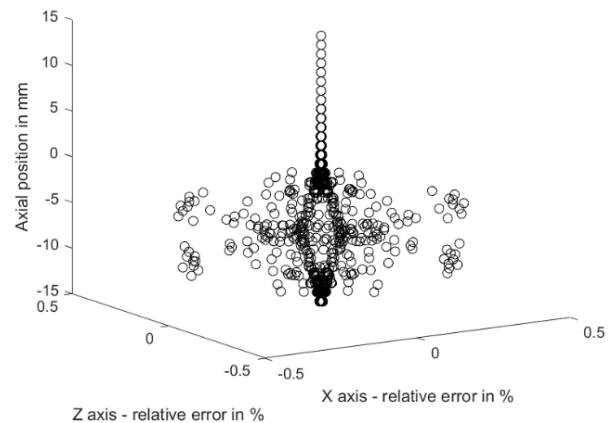


Figure 12: Relative difference between the mV/V output of the dynamometer with and without strain gauges

The difference between sensors output and analytical results was approximately 0.5 % with an associated standard deviation of the mean of 0.12 %.

## 4. DISCUSSIONS AND CONCLUSIONS

To put the results in the context, the relative uncertainty component associated with the force traceability was 20 ppm, which corresponds to 24 nV/V at 20 kN.

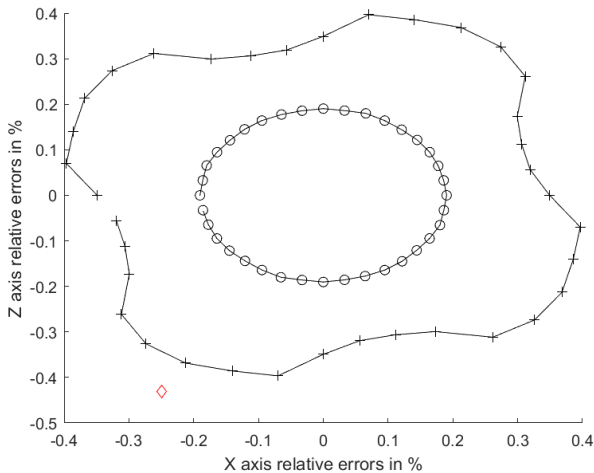


Figure 13: Relative difference between the mV/V output of the dynamometer with (+) and without strain gauges (o), average sensor output (◇) and the analytical solution

From the outset of section 3.1, the FEM results demonstrated their advantage over the analytical formulation to represent closely the dynamometer response, especially when the shape of the elastic element is not a perfect cylinder. The differences between the FEM and analytical solution, depicted in Figure 6, are always larger than the standard deviation associated with the FEM results, the standard deviation in this case being a measure of the effect of the spatial reproducibility FEM results. However, FEM requires very careful implementation which is especially important in the DT of measurement uncertainty context, from meshing to sampling and from choosing the correct constitutive models to extract/ visualise the results. For example, in this study only two node distances were studied, 2.5 mm and 1 mm, simulations form smaller meshing distances being nearly impossible to run in an average computer. The difference between the results obtained for these two meshing conditions being comparable with the top end traceability contribution (see Figure 7 and Figure 8). Much larger differences in results were recorded for different loading conditions, with magnitudes in the order of tens of a percentage at the lower end of the dynamometer to one percent of the reproduced values at the top end, as shown in Figure 9, highlighting potential effects of the loading set up.

However, the mV/V equivalent results present less errors compared to the individual strain values from which they are derived, as shown in Figure 10, highlighting the potential numerical errors arising from the approximations performed in FEM, and in

this case their effect on the radial position of the surface nodes. The way in which the sensors are connected in practice to measure the force without the bending effect seems to remove the effect of the FEM numerical errors.

Nevertheless, the sensor calibration results did not match the expected non-linear behaviour of the mV/V output (see Figure 11). This discrepancy is likely to originate from the strain gauges output, which has been addressed in section 3.2. The FEM results are affected by the presence of the strain gauges as shown in Figure 12 and Figure 13, which may change significantly with the type of constraint, subject of future work. However, the FEM non-linear errors do not change in the presence of the gauges attached to the dynamometer, meaning that the present configuration of the FEM is not able to predict current behaviour of the sensor.

Here we have investigated the FEM potential to become an integral part of a metrological DT [6] of a force device and, besides the discrepancies between the experimental and analytical results which require further investigations, we have shown that the FEM results can be used to provide reach graphical representation of the sensors output, which in turn can be used in future decision-making processes. Nevertheless, the next steps are focused on the conceptualisation of the DT [7], i.e. integrating the FEM model into a metrology decision making process.

## 5. ACKNOWLEDGEMENT

This work was funded by the European Metrology Program for Innovation and Research (EMPIR) in the Joint Research Project 18SIB08 ComTraForce.

## 6. REFERENCES

- [1] NASA, “NASA Technology Roadmaps TA11 - Modeling, Simulation, Information Technology and Processing”, 2015.
- [2] H. Kagermann et al., “Recommendations for Implementing I4.0”, acatech., Berlin, 2013.
- [3] A. Nitschke et al., “Entwicklung eines Kraft-Transfornormals für die Kalibrierung zyklischer Kräfte in Werkstoffprüfmaschinen mit Quantifizierung parasitärer Einflussgrößen”, Sensoren und Messsysteme, 2022.
- [4] M. Smith, “ABAQUS/Standard User's Manual”, Version 6.9, Dassault Syst. Sim. Corp., USA, 2019.
- [5] ISO 376, “Metallic materials - Calibration of force-proving instruments used for the verification of uniaxial testing machines”, ISO, Switzerland, 2011.
- [6] F. Härtig, “VirtMet applications and overview”, Berlin, September 2021.
- [7] L. Wright, S. Davidson, “How to tell the difference between a model and a digital twin”, Adv. Model. and Simul. in Eng. Sci, vol. 7, no. 13, pp. 1-13, 2020.